Additive Manufacturing 33 (2020) 101181

Contents lists available at ScienceDirect

Additive Manufacturing

journal homepage: www.elsevier.com/locate/addma

Prediction of mechanical behavior of 3D bioprinted tissue-engineered scaffolds using finite element method (FEM) analysis

Anahita Ahmadi Soufivand[a,b], Nabiollah Abolfathi[b,**], Seyyed Ataollah Hashemi[b], Sang Jin Lee[a,*]

[a] Wake Forest Institute for Regenerative Medicine, Wake Forest School of Medicine, Medical Center Boulevard, Winston-Salem, NC, 27157, USA
[b] Biomedical Engineering Faculty, Amirkabir University of Technology, 424 Hafez Ave, Tehran, Tehran Province, 15916, Iran

ARTICLE INFO

Keywords:
3D printing
CAD/CAM
Finite element method
Scaffold
Tissue engineering
Regenerative medicine

ABSTRACT

Three-dimensional (3D) printing can be a promising tool in tissue engineering applications for generating tissue-specific 3D architecture. The 3D printing process, including computer-aided design (CAD), can be combined with the finite element method (FEM) to design and fabricate 3D tissue architecture with designated mechanical properties. In this study, we generated four types of 3D CAD models to print tissue-engineered scaffolds with different inner geometries (lattice, wavy, hexagonal, and shifted microstructures) and analyzed them by FEM to predict their mechanical behaviors. For the validity of computational simulations by FEM, we measured the mechanical properties of the 3D printed scaffolds. Results showed that the theoretical compressive elastic moduli of the designed constructs were 23.3, 56.5, 67.5, and 1.8 MPa, and the experimental compressive elastic moduli were 23.6 ± 0.6, 45.1 ± 1.4, 56.7 ± 1.7, and 1.6 ± 0.2 MPa for lattice, wavy, hexagonal, and shifted microstructures, respectively, while maintaining the same construct dimension and porosity. In addition, van der Waals hyperelastic material model was successfully utilized to predict the nonlinear mechanical behavior of the printed scaffolds with different inner geometries. These findings indicated that the CAD-based FEM prediction could be used for designing tissue-specific constructs to mimic the mechanical properties of targeted tissues or organs.

1. Introduction

Three-dimensional (3D) printing and additive manufacturing have been utilized to combine cells and biomaterials to bioengineer tissue or organ constructs for tissue engineering applications [1–3]. These cutting-edge technologies (also known as 3D bioprinting) could precisely deposit multiple components, including tissue-specific cell types, biomaterials, and bioactive factors, in a micro-scale 3D architecture [4]. One of the most common methods for 3D bioprinting is based on microextrusion, during which material is extruded from the micron-scaled nozzle by pneumatic, piston, or screw-based dispensing system [5]. This microextrusion-based printing method requires melted thermoplastic polymers or polymer solutions with proper rheological properties. Among the polymeric materials available for 3D bioprinting purpose, poly(ε-caprolactone) (PCL) is the most commonly used polymer for the microextrusion bioprinting because of its low melting point of 60 °C and high printability [6]. However, 3D printed PCL-based scaffolds have a limited range of mechanical properties for tissue engineering applications. The mechanical signaling from tissue-engineered scaffolds could influence cellular activities, including proliferation and differentiation, as well as tissue hemostasis and development [6–9]. Thus, the mechanical properties of the scaffolds should be considered on the basis of the targeted tissues [10–12]. To address this, scaffold design strategies could be utilized to enhance the availability of PCL-based scaffolds that could provide significantly different mechanical properties.

The finite element method (FEM), which is a numerical method to model different domains, is a powerful tool to design 3D tissue architectures [13–15]. The FEM significantly improves the methodology in the design process for medical applications and is utilized in the analysis and design of orthopedic devices, as well as analysis of tissue growth [15]. Moreover, it has been used for understanding the biomechanical properties of targeted bioengineered tissue constructs and cell fate predictions to design and optimize the tissue-engineered scaffolds [8]. Due to the ability of CAD-based FEM method to provide high

* Corresponding author at: Wake Forest Institute for Regenerative Medicine, Wake Forest School of Medicine, Medical Center Boulevard, Winston-Salem, NC, 27157, USA.
** Corresponding author at: Biomedical Engineering Faculty, Amirkabir University of Technology, 424 Hafez Ave, Tehran, Tehran Province, 15916, Iran.
E-mail addresses: nabolfathi@aut.ac.ir (N. Abolfathi), sjlee@wakehealth.edu (S.J. Lee).

https://doi.org/10.1016/j.addma.2020.101181
Received 12 October 2019; Received in revised form 19 February 2020; Accepted 8 March 2020
Available online 19 March 2020

accuracy on designing and controlling the geometric configuration, and the ability of 3D printing to offer high reproducibility on the deposition of material, utilizing FEM capability to predict the mechanical behaviors of the scaffolds could be useful for the tissue-specific applications [16,17]. Through FEM capability in design, analysis, and prediction, tissue-specific scaffolds could be identified, and this approach may lead to accelerating the progression pace of the efforts to bioengineer tissue constructs using 3D bioprinting technologies.

In this study, we aimed to investigate the applicability of CAD-based FEM analysis to tune and predict the mechanical behaviors of the printed PCL scaffolds based on the inner geometries, as the inner geometries of the tissue-engineered scaffolds play an important role in biomechanical and biological aspects for tissue engineering applications [6,13,18]. We hypothesized that the controlled mechanical properties of tissue-engineered scaffolds fabricated by 3D printing could be obtained through designing different inner geometries via the FEM method. By using the computer-aided tissue engineering (CATE) approach, four types of tissue-engineered scaffolds with different mechanical properties were designed by different inner geometries (lattice, wavy, hexagonal, and shifted microstructures) using CAD-based FEM method. To validate the FEM prediction, the scaffolds with different inner geometries were fabricated by the extrusion-based 3D printing method and examined by the compression test. The entire processes established in FEM analysis are shown in Fig. 1.

2. Materials and methods

2.1. CAD-based scaffold design

We designed four types of tissue-engineered scaffolds with different microstructural patterns (lattice, wavy, hexagonal, and shifted). 3D CAD models of these scaffolds were generated using SolidWorks® (Dassault Systèmes SolidWorks Corp., Waltham, MA, USA). The porosity of each scaffold was calculated from the CAD model through two different approaches (designed and theoretical) as follows.

Designed porosity, the porosity of the CAD model, was obtained by measuring the occupied volume of each scaffold (V_{CAD}). The 3D CAD models were evaluated with SolidWorks software tools, and the design porosity (P_{CAD}) was calculated by Eq. 1:

$$P_{CAD} = (1 - \frac{V_{CAD}}{V_{Bulk}}) \times 100 \quad (1)$$

In which, V_{Bulk} is the bulk volume of the CAD model without porosity.

Theoretical porosity was estimated by considering the contact between the filaments of different layers to be only superficial [19]. This porosity contains the extra volume of material that existed in the overlapped regions that are neglected in the designed porosity calculation. To calculate the theoretical porosity, the scaffold layers were separated from each other in the CAD model to remove layer penetration and have superficial contact between filaments. Then the theoretical volume (V_{Theory}) of each scaffold was evaluated by SolidWorks software tools, and theoretical porosity (P_{Theory}) was calculated from Eq. 2:

$$P_{Theory} = (1 - \frac{V_{Theory}}{V_{Bulk}}) \times 100 \quad (2)$$

In which, V_{Bulk} is the bulk volume of the CAD model without porosity. Therefore, it is expected that the CAD porosity can be slightly higher than theoretically determined, and the theoretical porosity is more closely resembles printed porosity.

2.2. Tensile testing of the printed PCL filament

For FEM analysis, the tensile testing was performed according to ASTM D412-06a. A straight filament of poly(ε-caprolactone) (PCL, Mw 43,000–50,000; Polysciences, Warrington, PA, USA) were fabricated by a 3D printer, and the mechanical parameters were measured by a tensile tester. Instron 5544 (Instron, Norwood, MA, USA) was used for the tensile test using a 10 N load cell and loading rate of 5 mm/min. The length of the printed PCL filament was 5 cm, and the mean diameters were from 210.90–225.46 μm. The slope of the initial linear region of

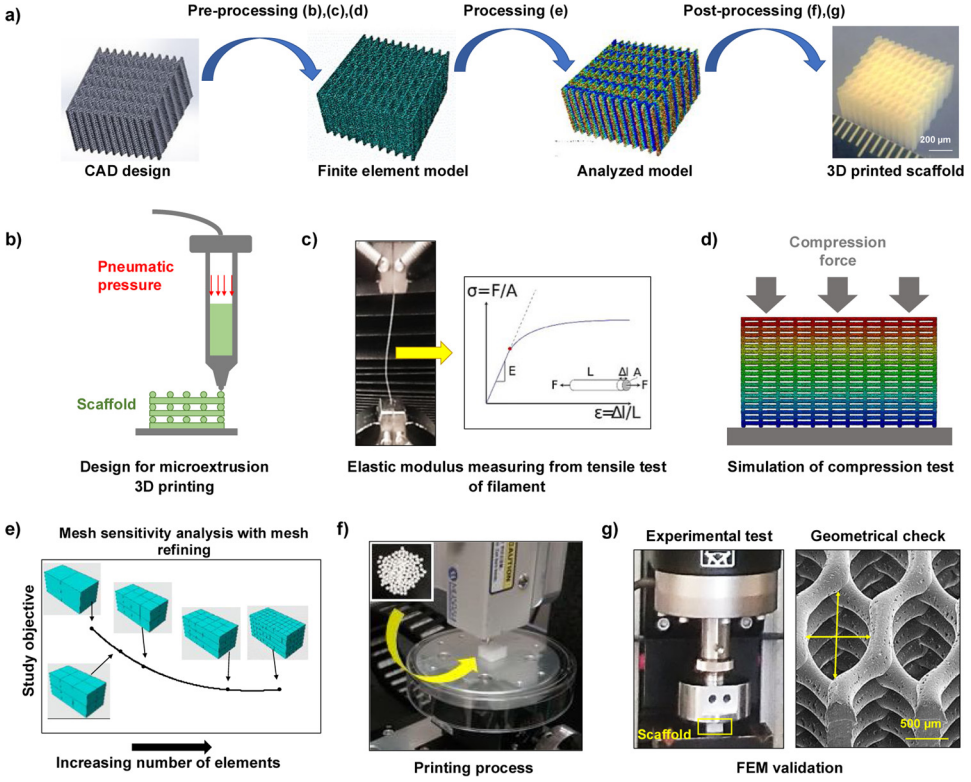

Fig. 1. Schematic diagram of the FEM process. (a) Main steps of FEM analysis: Pre-processing step to convert CAD model to FEM model: (b) design of the scaffold with CAD tool for manufacturing with the microextrusion 3D printing, (c) determination of mechanical properties of PCL filament by tensile testing for FEM model, (d) simulation of the boundary condition of the scaffold under unidirectional compression; Processing step to analyze FEM model: (e) mesh sensitivity analysis of FEM model with increasing the number of elements (mesh refining) to have mesh independent numerical results; and Post-processing step to validate FEM analysis: (f) 3D printing process with optimized parameters and (g) validation of FEM results with the experimental results obtained from unidirectional compression test of the 3D printed scaffolds and measurement of the geometrical specifications using SEM images.

the stress-strain curve was considered as the elastic modulus. Based on the stress-strain curve, the elastic modulus of the PCL filament, E_F, was calculated by Eq. 3.

$$E_F = \frac{4F_t \times L}{\pi D^2 \times \Delta L} \tag{3}$$

In which F_t is the tensile force, L is the length of the filament, D is the diameter of the filament, and ΔL is the tensile extension of the filament.

In order to have a constant diameter of the testing samples, the mean diameter of each filament (D_{mean}) was used in Eq. 2. According to the standard ASTM D412-06a recommendation, the weight of each sample (M) was measured, and the mean diameter was calculated by Eq. 4.

$$D_{mean} = 2\sqrt{\frac{M}{\rho L \pi}} \tag{4}$$

In which ρ is the density of PCL material which is 1.145 g/cm^3, and L is the length of the filament.

2.3. Finite element method (FEM) modeling

We used ABAQUS/Standard® 6.13 (Simulia, Dassault Systèmes) finite element package to predict the mechanical behavior of the designed tissue-engineered scaffolds under compression. To generate FEM models in the preprocessing stage, the 3D CAD model of each scaffold was imported into the software as a continuous part. The material properties of PCL were simulated by both linear and nonlinear elastic behavior. The FEM model specifications for both linear and nonlinear analyses were similar, but only the material definition was different between them. In the next step, nodes and mesh regions on the FEM model of each scaffold were generated from the initial continuous model. Ten nodes of quadratic tetrahedral elements with four integration points denoted by C3D10 in Abaqus were used based on the geometry of each FEM model. One of the considerable aspects of FEM analysis is the dependency of its result accuracy on the mesh size since the FEM model with coarse mesh is not representative of the continuous model and leads to deviation from exact results. Thus, a mesh sensitivity analysis was performed with constantly decreasing the mesh size (or increasing the number of elements) to reach mesh size-independent results. After performing this analysis, a suitable mesh size on the FEM models was obtained for the following FEM analysis.

Linear elastic material properties in FEM are defined by two parameters; elastic modulus and Poisson's ratio. In this study, the elastic modulus was obtained by measuring tensile properties of a printed filament as described in the following section, and the value of Poisson's ratio was assumed 0.3 according to the previous report [16]. The compression testing simulation was completed by the FEM analysis of each scaffold design. Especially, the compressive elastic modulus was compared with the scaffolds designed by CAD, which is the most considerable mechanical properties of tissue-engineered scaffolds [20–22]. Subsequently, to simulate the uniaxial compression test in the static analysis, the 5% compressive strain was exerted to the top of the model, and the bottom of the part was fixed as boundary conditions. The compression force was obtained for each scaffold in the post-processing stage. Then, compressive elastic modulus, E_{FEM}^{com}, was obtained from Eq. (5):

$$E_{FEM}^{com} = \frac{F_{FEM}^{com}}{A \times \varepsilon_{FEM}^{com}} \tag{5}$$

In which, F_{FEM}^{com} is compression force at the end of the analysis, A is the initial area under compression, and ε_{FEM}^{com} is a compressive strain of 5%.

For nonlinear elastic behavior, the compressive mechanical behavior of each scaffold was predicted in higher strain ranges by using the three nonlinear hyperelastic material models, Neo Hooke, Mooney-Rivlin, and van der Waals [23]. Their strain energy functions are:

$$(\text{Neo Hooke})\, U = C_{10}(\bar{I}_1 - 3) + \frac{1}{D}(J_{el} - 1)^2$$

$$(\text{Mooney–Rivlin})\, U = C_{10}(\bar{I}_1 - 3) + C_{01}(\bar{I}_2 - 3) + \frac{1}{D}(J_{el} - 1)^2$$

$$(\text{van der Waals})\, U = \mu\left\{-(\lambda_m^2 - 3)[\ln(1-\eta) + \eta] - \frac{2}{3}a\left(\frac{\bar{I} - 3}{2}\right)^{\frac{3}{2}}\right\} + \frac{1}{D}\left(\frac{J_{el}^2 - 1}{2} - \ln J_{el}\right)$$

$$\bar{I} = (1-\beta)\bar{I}_1 + \beta\bar{I}_2 \text{ and } \eta = \sqrt{\frac{\bar{I} - 3}{\lambda_m^2 - 3}}$$

where U is the strain energy potential, J_{el} is the elastic volume ratio, $\bar{I}_1$ and $\bar{I}_2$ are the first and second invariants of the deviatoric strain, and C_{10}, C_{01}, μ, λ_m, a, β, and D are material constants. C_{10} and C_{01} describes the shear behavior of the material, μ, λ_m, a and β describe the deviatoric behavior, and D introduces compressibility.

To obtain the hyperelastic parameters, the initial values were estimated using the Abaqus material evaluation option base on available uniaxial tensile test data and Poisson's ratio of 0.3 for PCL material. These initial values were modified by simulating the uniaxial tensile test of PCL filament in Abaqus and trial-and-error procedure to reach an appropriate fit to the experimental data and have stable material behavior in large deformation. In addition, this relation between compressibility (D), initial bulk (K_0), and shear modulus (μ_0) must be existed [24,25] in all hyperelastic models:

$$D = \frac{2}{K_0} = \frac{3(1-2\upsilon)}{\mu_0(1+\upsilon)}$$

Instead, the initial shear modulus has a relationship with the hyperelastic parameters as follows:

$$(\text{Neo Hooke})\, \mu_0 = 2C_{10}$$

$$(\text{Mooney–Rivlin})\, \mu_0 = 2(C_{10} + C_{01})$$

$$(\text{van der Waals})\, \mu_0 = \mu$$

Thus, the relationships between the compressibility and material parameters are:

$$(\text{Neo Hooke})\, D = \frac{3(1-2\upsilon)}{2C_{10}(1+\upsilon)}$$

$$(\text{Mooney–Rivlin})\, D = \frac{3(1-2\upsilon)}{2(C_{10} + C_{01})(1+\upsilon)}$$

$$(\text{van der Waals})\, D = \frac{3(1-2\upsilon)}{\mu(1+\upsilon)}$$

After reaching appropriate material parameters, the apparent compressive stress-strain curve for each scaffold was obtained and compared with the experimental data. Afterward, shear moduli of scaffolds with four types of microstructures were estimated. The shear strain (γ_{shear}) was exposed to the top layer of the scaffold, shear force (F) were calculated from FEM analysis and the apparent shear modulus (G) was calculated with Eq. 6:

$$G = \frac{F}{A\gamma_{shear}} \tag{6}$$

2.4. 3D printing of the tissue-engineered scaffolds

To validate the FEM prediction, each scaffold was fabricated by the microextrusion-based printing method based on the CAD design. In this study, we used the integrated tissue-organ printing (ITOP) system

developed in our group [4]. Custom-made computer-aided manufacturing (CAM) software-generated G-code, which instructed the bioprinter on how to print the scaffolds with different inner geometries. The PCL granules were melted at 90 °C for 30 min and dispensed through a metal syringe. The metal syringe was fitted with a stainless-steel nozzle with an internal diameter of 200 μm. All scaffolds were printed with 200 mm/min of the scan speed. In the printing pressure, lattice and shifted microstructures were printed at 350 kPa, and wavy and hexagonal were printed at 400 kPa. The dimension of the printed scaffolds was 6 (H) × 10 × 10 mm^3 for the following mechanical testing according to ISO 604 recommendation [26].

2.5. Characterizations of the printed scaffolds

The printed scaffolds were morphologically characterized using a high-resolution emission scanning electron microscope (SEM, Hitachi FlexSEM, model SU 1000, Japan). The samples were pre-coated with a conductive layer of sputtered gold-palladium in a sputter coater (EM ACE600, Leica). SEM micrographs were taken at an accelerating voltage of 10.0 kV at different magnifications and analyzed by Image-Pro software (Media Cybernetics, Rockville, MD, USA). The porosity ($\boldsymbol{P_{3DP}}$) of each scaffold was calculated by the following Eq. 7:

$$\boldsymbol{P_{3DP}} = (1 - \frac{\boldsymbol{M}}{\boldsymbol{\rho V_{Bulk}}}) \times 100 \quad (7)$$

In which $\boldsymbol{M}$ is the weight of the sample, $\boldsymbol{\rho}$ is the PCL density which is 1.145 g/cm^3, and $\boldsymbol{V_{Bulk}}$ is the bulk volume of the CAD part without porosity. The SEM measurements were performed randomly from different regions of images.

The mechanical properties of the printed scaffolds with different microstructural patterns were measured with a universal mechanical testing machine (Instron 5544) under compression (2 kN load cell and 0.2 mm/min) according to ISO604 recommendation. At least five samples were tested with each scaffold.

2.6. Statistical analysis

Data were analyzed with Student's *t*-test or one-way ANOVA using GraphPad Prism software version 5.0 (GraphPad Software, Inc., La Jolla, CA). $P < 0.05$ was considered statistically significant.

3. Results

3.1. CAD-based scaffold design

After preparing several CAD designs for the scaffold, four designs with specific microstructures were chosen based on design prerequisites. Fig. 2 shows the design parameters and microstructural patterns. The lattice-micropatterned scaffold was used as a control because this structure is common in 3D bioprinting applications. To design scaffolds with different mechanical properties, the amount of contact area between layers was considered. Wavy and hexagonal-micropatterned scaffolds were assumed to have higher contacting regions between layers. These contacting regions resulted in thick, straight columns within the scaffolds. However, the shifted-micropatterned scaffold showed limited contacting regions. For lattice, wavy, and hexagonal geometries, the scaffold consisted of 20 repetitions of 2 layers, and the shifted-micropatterned scaffold consisted of 10 repetitions of 4 layers. To apply the compression displacement to the top layer of each model and fix the bottom layer, the layers were cut 20 μm in the horizontal direction. The designed scaffold size was based on ISO 604. The CAD models of each scaffold were prepared with dimensions of 6 (H) × 10 × 10 mm^3. All scaffolds were highly porous with similar porosity.

3.2. FEM model preparation and mesh sensitivity analysis

Compression tests were simulated by defining boundary conditions representative of the actual compression tests. The CAD model was converted to the FEM model by defining the boundary condition and generating a 3D mesh (Fig. 3a,b. In addition, a mesh refining process was performed, and a sufficient number of elements and mesh size were generated on FEM models 1,894,283 for lattice, 1,026,865 for wavy, 5,146,087 for hexagonal, and 1,965,574 for shifted. Fig. 3c shows the result of mesh sensitivity analysis for the hexagonal-micropatterned scaffold as an example.

3.3. FEM analysis

For linear FEM analysis, the elastic modulus of PCL filament was calculated by the slope of the initial linear region of the stress-strain curve. The representative elastic modulus was 431.5 ± 10.2 MPa. The elastic modulus was used in the FEM models with the assumption of linear elastic deformation. Using the elastic modulus obtained from the PCL filament, FEM analysis was performed for each scaffold, and the mechanical behavior under compression was simulated. Fig. 4 shows the distribution of Von-Mises Stress as a valuable quantity for comparing the scaffolds with different geometries. This indicates that the vertical supportive column plays an important role in the resistance of the scaffolds to a compressive load. In addition, the number of maximum stresses was the same for lattice, wavy, and hexagonal micropatterned scaffolds, and the increase of compressive elastic modulus in wavy and hexagonal micropatterned scaffolds in comparison of lattice scaffold could be due to the existence of more thick columns in the scaffolds. The amount of maximum stress for the shifted scaffold was lower compared with other scaffolds due to the absence of a supportive column. Using the FEM simulation, the amount of force after completion of analysis was obtained, and the equivalent compressive elastic modulus was calculated by the ratio of compressive stress to compressive strain.

In addition, shear moduli of each microstructure were estimated by simulating shear test on each scaffold in two lateral directions. The von-Mises stress-strain distribution and the amount of shear modulus in each direction are depicted in Fig. 5a,b. The value of shear modulus for lattice and shifted microstructures has no directional dependency because of symmetry in their geometries. But for wavy and hexagonal microstructures, the shear moduli values are highly directional dependence. Eventually, the lateral compressive elastic moduli of each microstructure were estimated using FEM and shown in Fig. 5c. Lateral elastic moduli in two directions were similar for both lattice and shifted microstructures because of their geometrical symmetry in these directions. Unlike, both wavy and hexagonal microstructures have the uneven elastic modulus in lateral directions. The results show that all microstructures have a directional dependency and their axial and lateral elastic moduli were different. It is more significant in wavy and hexagonal types of microstructures.

For nonlinear FEM analysis, the tensile behavior of PCL filament was predicted using the hyperelastic models. The numerical and experimental stress-strain curves were plotted in Fig. 6. The material parameters which were used to describe these three hyperelastic models are listed in Table 1.

Based on this prediction, the compressive behavior of lattice microstructure was predicted using hyperelastic models and compared by experimental data after the characterization of the printed scaffolds in the following section to choose the best model between these three models. Moreover, using the selected model, the mechanical behavior of other microstructures under compression was predicted numerically and compared by experiment.

a)

Filaments distance, S, (μm)	Filament size, D, (μm)	Layer height, H, (μm)	Number of layers	Angle of pattern, A, (degree)
700	200	150	40	45

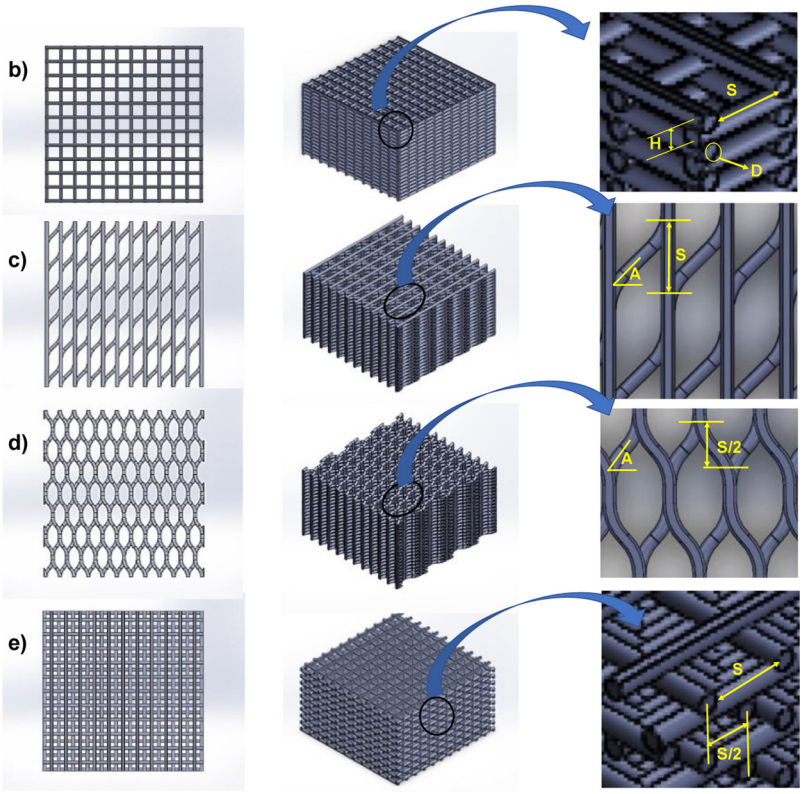

Fig. 2. CAD designs of four types of micropatterns for the tissue-engineered scaffolds. (a) Designed geometric information of the scaffolds. Top and 3D views of designed micropatterns in the scaffolds: (b) lattice (c) wavy, (d) hexagonal, and (e) shifted.

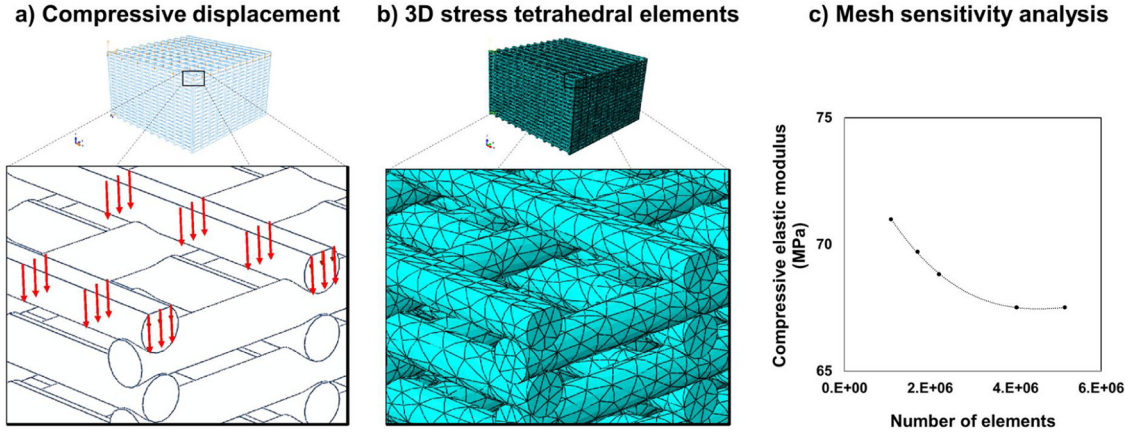

Fig. 3. Preparation of FEM model for analysis. (a) Defining of the loading condition in accordance with the actual unidirectional compression by exerting the compressive displacement on the top layer of the scaffold equal to 5% and 10 % strain for linear and nonlinear FEM analyses, respectively, (b) mesh generation on the scaffold model using 3D stress tetrahedral (C3D10) elements to prepare FEM model for further analysis, and (c) mesh sensitivity analysis results for the hexagonal scaffold as an example. This analysis was also performed for lattice, wavy, and shifted micropatterned scaffolds to obtain the mesh independent results. The number of elements was increased until steady numerical results were reached.

3.4. Characterizations of the printed scaffolds with different inner geometries

Fig. 7 shows the gross appearance of the printed scaffolds and SEM images from the surface and cross-section of scaffolds. In the cross-sectional SEM images, the filament distances were 682.9 ± 2.6, 664.2 ± 8.0, 658.8 ± 3.2, and 658.1 ± 1.8 μm, and layer heights were 151.5 ± 3.7, 158.3 ± 3.0, 157.1 ± 0.9, and 153.7 ± 1.4 for lattice, wavy, hexagonal, and shifted geometries, respectively (Table 2). This indicates that the filaments were placed in scaffold accurately similar to CAD designs with the filament distance of 700 μm and the layer height of 150 μm. The dimension of each scaffold was also measured by digital caliper, and they were printed accurately which were very similar to the designed dimension. The results showed that the geometrical dimensions were similar to designed values as analyzed by the FEM simulation (Table 2).

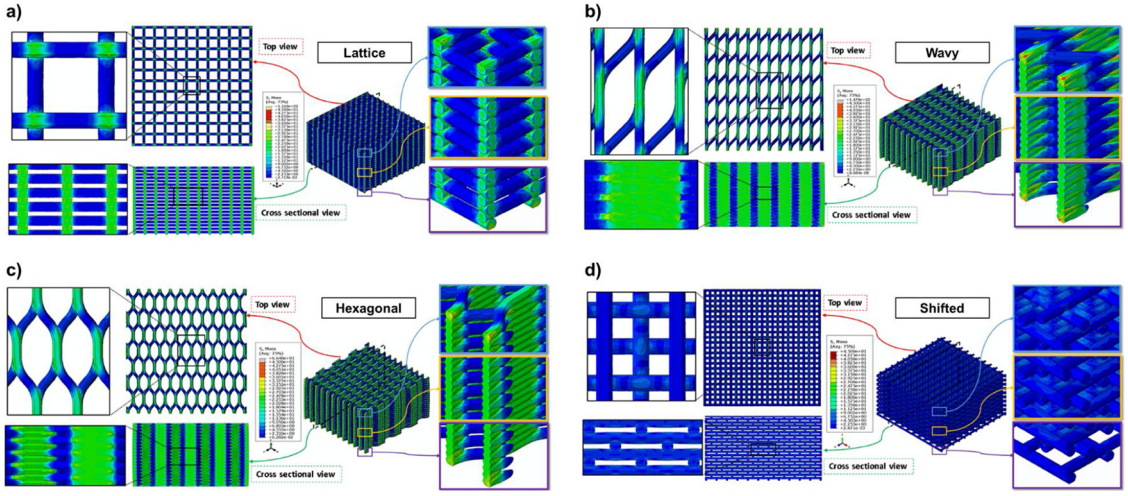

Fig. 4. Contour plots of Von-Mises Stress and distribution in FEM models of four microstructures: (a) lattice, (b) wavy, (c) hexagonal, and (d) shifted. The stress value increases from blue to red colors.

Fig. 8a shows the representative stress-strain curves of the scaffolds with four types of inner geometries. The compressive elastic moduli of the wavy and hexagonal micropatterned scaffolds were significantly higher than that of the lattice-micropatterned scaffold (45.1 ± 1.4 MPa for wavy and 56.7 ± 1.7 MPa for hexagonal vs. 23.6 ± 0.6 MPa for lattice, $^{*}P < 0.05$, Fig. 8b and Table 3). The shifted-micropatterned scaffold showed the decrease of the compressive elastic modulus (1.6 ± 0.2 MPa) when compared with the lattice-micropatterned scaffold.

To validate the linear FEM simulation, the numerical theoretical and experimental values were compared (Table 3). The results show that the FEM method is a powerful tool to predict elastic modulus of the printed scaffolds, especially, in the microstructures with a lower degree of complexity like lattice and shifted scaffolds. The elastic modulus from linear FEM results for wavy and hexagonal scaffolds was in a range of 16–20 % in comparison with experimental results.

The nonlinear FEM analysis was evaluated by comparing its predictions with experimental data (Table 3). The predictions of hyperelastic models to describe the compressive behavior of lattice microstructure are depicted in Fig. 9a. Van der Waals model better described the material behavior of PCL filament (R^2 = 0.99, 0.98 and 0.98 for Van der Waals, Neo Hooke, and Mooney-Rivlin, respectively, Fig. 6) and lattice microstructure (R^2 = 0.98, 0.92 and 0.91 for Van der Waals,

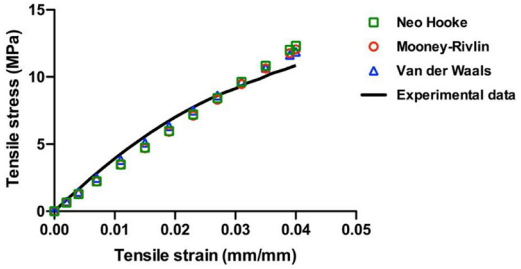

Fig. 6. Prediction of tensile behavior of PCL filament using Neo Hooke, Mooney-Rivlin, and Van der Waals models in comparison with experimental data. All data are represented as the average values from n = 5 per group.

Table 1
Utilized material parameters of different hyperelastic models to describe the nonlinear mechanical behavior of PCL filament.

Neo Hooke	$\boldsymbol{C}10 = 60$, $\boldsymbol{D} = 0.00769$
Mooney-Rivlin	$\boldsymbol{C}10 = 20$, $\boldsymbol{C}01 = 40$, $\boldsymbol{D} = 0.00769$
van der Waals	$\boldsymbol{\mu} = 140$, $\boldsymbol{\lambda_m} = 1.9$, $\boldsymbol{a} = 6$, $\boldsymbol{\beta} = 0$, $\boldsymbol{D} = 0.00659$

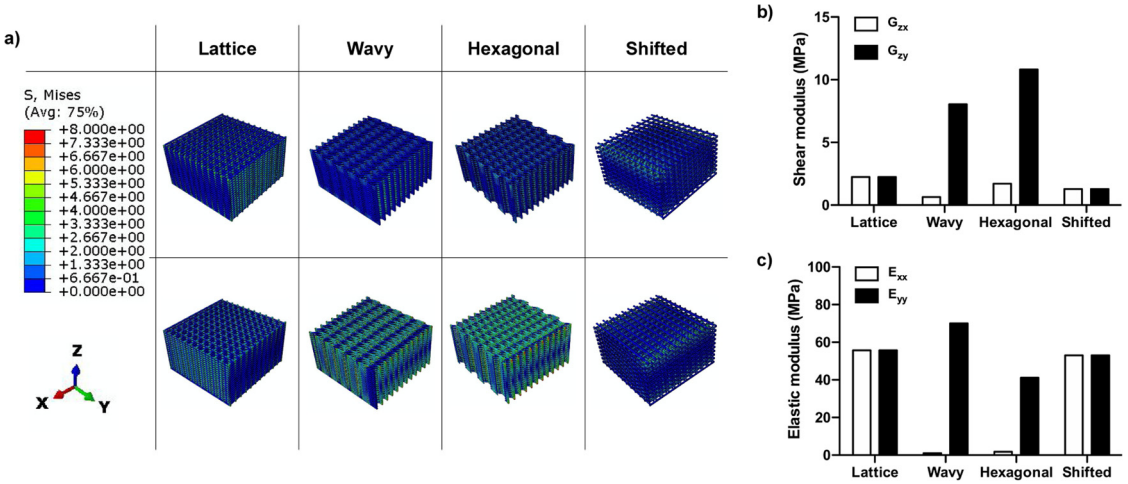

Fig. 5. (a) The Von-Mises stress-strain distributions in the simulated shear test by FEM in two lateral directions (x,y). Estimation of (b) shear moduli and (c) elastic moduli of scaffolds with different microstructures.

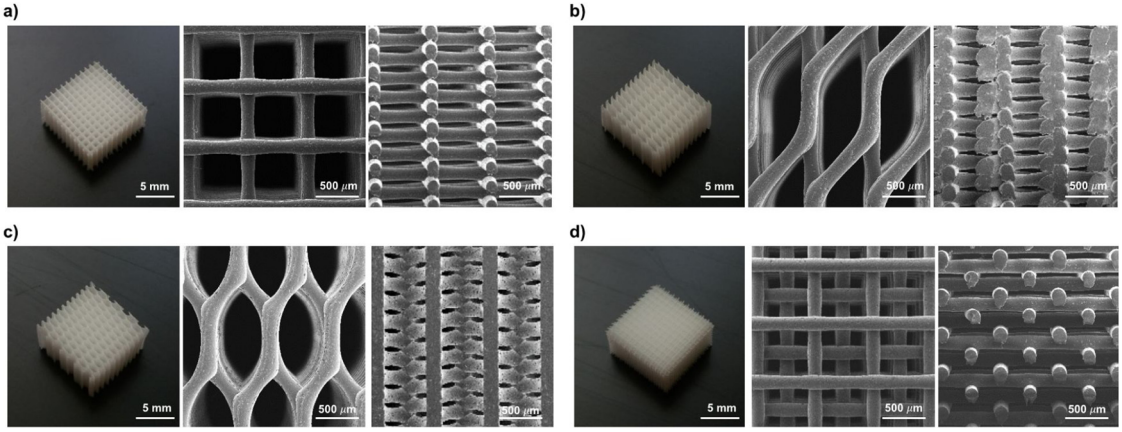

Fig. 7. Gross and SEM images of the 3D printed scaffolds with different inner geometries: (a) lattice, (b) wavy, (c) hexagonal, and (d) shifted.

Table 2
Comparison of CAD and experimental results of four types of scaffolds with different inner geometries.

	CAD filament distance, S (μm)	SEM filament distance, S (μm)	CAD layer height, H (μm)	SEM layer height, H (μm)	CAD angle of pattern, A (degree)	CAD angle of pattern, A (degree)	CAD porosity, P_{CAD} (%)	Theoretical porosity, P_{Theory} (%)	Experimental porosity, P_{3DP} (%)
Lattice	700	682.9 ± 2.6	150	151.5 ± 3.7	–	–	75.9	75.3	74.7 ± 0.5
Wavy	700	664.2 ± 8.0	150	158.3 ± 3.0	45	45.6 ± 0.5	75.4	73.7	68.4 ± 0.6
Hexagonal	700	658.8 ± 3.2	150	157.1 ± 0.9	45	44.6 ± 1.2	76.2	74.5	68.7 ± 0.4
Shifted	700	658.1 ± 1.8	150	153.7 ± 1.4	–	–	76.9	76.3	76.2 ± 0.6

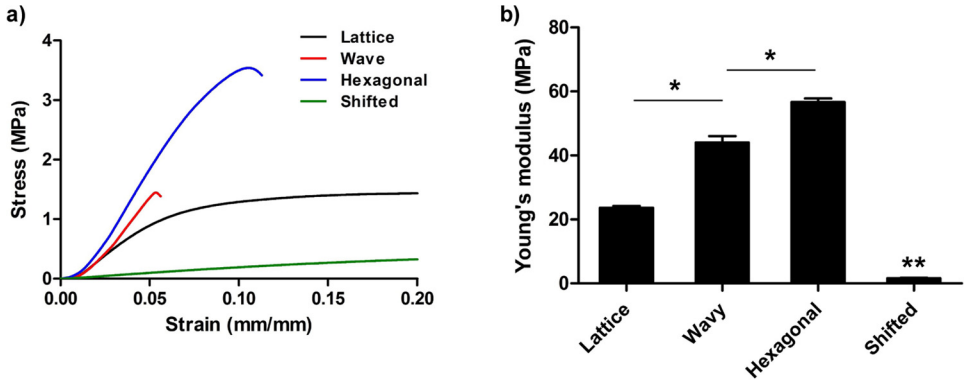

Fig. 8. The compression testing of scaffolds with different inner geometries: lattice, wavy, hexagonal, and shifted. (a) Representative compressive stress-strain curves and (b) Young's modulus (compressive elastic modulus). All data are represented as mean ± SD (n = 5, $^*P < 0.05$ and $^{**}P < 0.05$ compared with lattice scaffold).

Table 3
Compression elastic moduli from the linear model and initial elastic modulus from van der Waals nonlinear model in comparison with experimental elastic moduli.

FEM linear model, E_{FEM}^{com} (MPa)	FEM nonlinear model - van der Waals, E_{FEM}^{com} (MPa)	Experimental, E_{Exp}^{com} (MPa)
23.3	19.8	23.6 ± 0.6
56.5	50.6	45.1 ± 1.4
67.5	56.1	56.7 ± 1.7
1.8	1.5	1.6 ± 0.2

Neo Hooke, and Mooney-Rivlin, respectively, Fig. 9a) in comparison to Neo Hooke and Mooney-Rivlin models. Thus, van der Waals model was chosen as an appropriate material model for PCL filament, and nonlinear FEM analysis of remaining microstructures was conducted using this model. The predicted compressive strain-stress curves in comparison with experimental data for wavy, hexagonal and shifted microstructures are plotted in Fig. 9b.

The nonlinear FEM results show that this method is highly applicable to predict the mechanical properties of the printed scaffolds under compression beyond the linear region. The hyperelastic material model was successfully used in FEM analysis to predict the behavior of four microstructures and there were good correlations between experimental and numerical data (R^2 = 0.98, 0.91, 0.98, and 0.99 for lattice, wavy, hexagonal and shifted, respectively). Moreover, the initial elastic modulus was in an acceptable range in comparison with the experimental elastic modulus. Initial elastic moduli from the nonlinear analysis were closer to experiment than elastic moduli from linear analysis for all microstructures except lattice microstructure.

4. Discussion

The FEM simulation can be a powerful tool to determine the mechanical behaviors of materials, including force, deformation, stress, strain, elastic modulus, and strength in different loading regime, including compression, tension, bending, fatigue, and fracture under static and dynamic states [27,28]. Moreover, structural, thermal, and fluid mechanics can be analyzed by this method [29,30]. Thus, the FEM method combined with 3D bioprinting technologies has the potential to

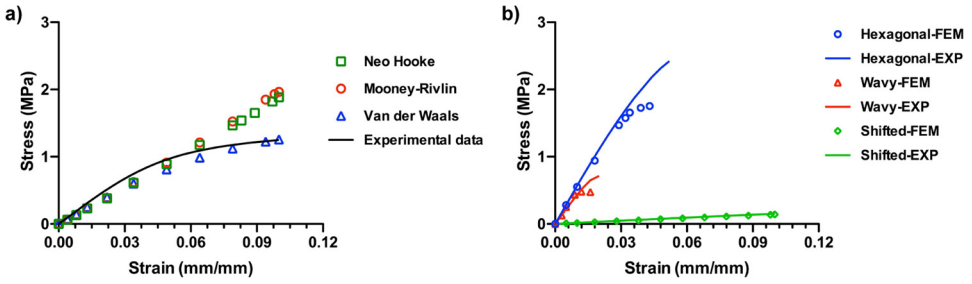

Fig. 9. (a) Prediction of nonlinear compressive behavior of lattice microstructure using Neo Hooke, Mooney-Rivlin, and van der Waals hyperelastic models and comparison with unidirectional compression experimental data. (b) Prediction of the nonlinear compressive behavior of wavy, hexagonal and shifted microstructures using van der Waals hyperelastic model for the printed scaffolds. All data are represented as the average values from $n = 5$ per group.

predict the scaffold's properties under various physiological and biomechanical conditions. In this study, four types of tissue-engineered scaffolds with different inner geometries were designed by 3D CAD-based FEM analysis. The designed porosity of the scaffolds was higher than 70 %, which could facilitate cell ingrowth, vascularization, and nutrition/oxygen supply.

Thermoplastic PCL, which was used as the scaffold material, is the most common polymer in 3D bioprinting applications. Since the melting process is required for the microextrusion printing method, PCL is exposed to thermal stresses, and its crystallinity degree can be changed during the printing process. Moreover, the thermal damage and crystallinity change led to variations in the elastic modulus after the printing. In this study, we maintained the same printing conditions for the scaffolds and total printing time was not exceeded more than 6 h to avoid thermal stresses to the PCL. In addition, the mechanical test was performed after 2 days of printing to stabilize the crystallinity of the PCL-based scaffolds. As a result, the elastic modulus between PCL filament and the scaffolds was converged to similar values (standard deviation of compressive elastic modulus was as low as 4% on average).

Using the FEM simulation, the compressive elastic moduli of the scaffolds with different inner geometries were predicted a broad range from 1.8–67.5 MPa. This range can be controlled by the design parameters such as pore size, porosity, layer height, material, and microstructure. We assumed that these design parameters could influence the bonding strength between layers and filaments in the printed scaffolds, and the layer bonding of the shifted scaffold could be significantly weaker than that of the lattice scaffold. Because every two layers shift, the layers were not printed repeatedly on each other, which could result in a decrease of the bonding strength. However, the wavy and hexagonal scaffolds had the extended bonded layer areas, resulting in an increase of the bonding strength.

Shear modulus was highly dependent on the type and direction of microstructure, and the hexagonal microstructure with the highest axial elastic modulus has the highest shear modulus in y-direction but the decreased value in x-direction. Moreover, shear modulus in y-direction was decreased from wavy and lattice to shifted microstructure similar to the axial compressive elastic modulus. Lateral elastic moduli for lattice and shifted microstructures were similar to their supporting columns to withstand the compression were the same. The wavy microstructure has the highest lateral elastic modulus in y-direction because of the highest amount of supporting column in this direction and the lowest elastic modulus in x-direction. Although the hexagonal microstructure showed the highest axial compressive elastic modulus in lateral directions, its elastic moduli were lower than lattice and shifted in both direction and wavy in y-direction.

In the nonlinear FEM analysis of the compression test, all models' predictions were similar in small strain ranges but, by increasing the strain value, van der Waals model better described the mechanical behavior of lattice microstructure. The results showed that PCL filament and the printed scaffold demonstrated the hyperelastic behavior under tension and compression, respectively. To better describe the nonlinearities in PCL material and to have a more complete material definition, analyzing experimental data from various modes of loading with higher ranges of strain should be beneficial.

This FEM method to predict the mechanical properties of the tissue-engineered scaffolds can be extended to utilize various polymeric materials under different physiological loading conditions based on the targeted tissues. In addition, the effect of the design parameters such as layer penetration, the dimension of printing path, and layers organization can be studied using this method to examine a relationship between each parameter and scaffold's properties. Ultimately, the automated strategy can be utilized to design and fabricate tissue-specific scaffolds by coupling optimization algorithms with the FEM method.

5. Conclusions

We utilized the FEM modeling to predict the compressive mechanical properties of the tissue-engineered scaffolds. Based on the 3D CAD design, the scaffolds with four types of inner geometries (lattice, wavy, hexagonal, and shifted) were fabricated by the microextrusion-based 3D bioprinting. The results showed that the numerical theoretical values were in good agreement with experimental values for both linear and nonlinear FEM analyses. Especially, van der Waals hyperelastic model simulated the material behavior of the PCL filament and printed scaffolds in small and large deformations very well. In addition, the different directional dependency of microstructures in terms of shear and elastic moduli was examined numerically. We demonstrated that the FEM method combined with 3D bioprinting has the potential to predict the mechanical properties of the scaffolds under load-bearing conditions without any fabrication. This approach could provide the design and fabrication strategies for tissue-specific scaffolding system in tissue engineering applications.

Author statement

A.A.S., N.A., and S.J.L. developed the concept and designed methodologies. A.A.S. performed all experiments. A.A.S., S.A.H., and S.J.L. analyzed data, and A.A.S. wrote the manuscript. S.J.L. edited the manuscript, and N.A., and S.J.L. provided the direction of the project. N.A. and S.J.L. acquired the financial support for the project.

Declaration of Competing Interest

The authors declare no competing financial interests.

Acknowledgments

This study was supported by the U.S. National Science Foundation (NSF, Award #1663128). A. A. S. was supported by the Iran Ministry of Science, Research, and Technology (MSRT) for providing a scholarship for research of Ph.D. student abroad.

Appendix A. Supplementary data

Supplementary material related to this article can be found, in the online version, at doi:https://doi.org/10.1016/j.addma.2020.101181.

References

[1] S.V. Murphy, A. Atala, 3D bioprinting of tissues and organs, Nat. Biotechnol. 32 (8) (2014) 773–785.
[2] Y.J. Seol, H.W. Kang, S.J. Lee, A. Atala, J.J. Yoo, Bioprinting technology and its applications, Eur. J. Cardiothorac. Surg. 46 (3) (2014) 342–348.
[3] A.A. Zadpoor, J. Malda, Additive manufacturing of biomaterials, tissues, and organs, Ann. Biomed. Eng. 45 (1) (2017) 1–11.
[4] H.W. Kang, S.J. Lee, I.K. Ko, C. Kengla, J.J. Yoo, A. Atala, A 3D bioprinting system to produce human-scale tissue constructs with structural integrity, Nat. Biotechnol. 34 (3) (2016) 312–319.
[5] I.T. Ozbolat, M. Hospodiuk, Current advances and future perspectives in extrusion-based bioprinting, Biomaterials 76 (2016) 321–343.
[6] A.D. Olubamiji, Z. Izadifar, J.L. Si, D.M. Cooper, B.F. Eames, D.X. Chen, Modulating mechanical behaviour of 3D-printed cartilage-mimetic PCL scaffolds: influence of molecular weight and pore geometry, Biofabrication 8 (2) (2016) 025020.
[7] L. Moroni, J.R. de Wijn, C.A. van Blitterswijk, 3D fiber-deposited scaffolds for tissue engineering: influence of pores geometry and architecture on dynamic mechanical properties, Biomaterials 27 (7) (2006) 974–985.
[8] W.J. Hendrikson, C.A. van Blitterswijk, J. Rouwkema, L. Moroni, The use of finite element analyses to design and fabricate three-dimensional scaffolds for skeletal tissue engineering, Front. Bioeng. Biotechnol. 5 (2017) 30.
[9] A.L. Olivares, E. Marsal, J.A. Planell, D. Lacroix, Finite element study of scaffold architecture design and culture conditions for tissue engineering, Biomaterials 30 (30) (2009) 6142–6149.
[10] A. Cheng, Z. Schwartz, A. Kahn, X. Li, Z. Shao, M. Sun, Y. Ao, B.D. Boyan, H. Chen, Advances in porous scaffold design for bone and cartilage tissue engineering and regeneration, Tissue Eng. Part B Rev. 25 (1) (2019) 14–29.
[11] S.J. Hollister, Porous scaffold design for tissue engineering, Nat. Mater. 4 (7) (2005) 518–524.
[12] J. Wieding, A. Wolf, R. Bader, Numerical optimization of open-porous bone scaffold structures to match the elastic properties of human cortical bone, J. Mech. Behav. Biomed. Mater. 37 (2014) 56–68.
[13] B. Ostrowska, A. Di Luca, K. Szlazak, L. Moroni, W. Swieszkowski, Influence of internal pore architecture on biological and mechanical properties of three-dimensional fiber deposited scaffolds for bone regeneration, J. Biomed. Mater. Res. A. 104 (4) (2016) 991–1001.
[14] L. Baldino, F. Naddeo, S. Cardea, A. Naddeo, E. Reverchon, FEM modeling of the reinforcement mechanism of Hydroxyapatite in PLLA scaffolds produced by supercritical drying, for Tissue Engineering applications, J. Mech. Behav. Biomed. Mater. 51 (2015) 225–236.
[15] A. Boccaccio, A. Ballini, C. Pappalettere, D. Tullo, S. Cantore, A. Desiate, Finite element method (FEM), mechanobiology and biomimetic scaffolds in bone tissue engineering, Int. J. Biol. Sci. 7 (1) (2011) 112–132.
[16] S. Eshraghi, S. Das, Micromechanical finite-element modeling and experimental characterization of the compressive mechanical properties of polycaprolactone-hydroxyapatite composite scaffolds prepared by selective laser sintering for bone tissue engineering, Acta Biomater. 8 (8) (2012) 3138–3143.
[17] S. Barui, S. Chatterjee, S. Mandal, A. Kumar, B. Basu, Microstructure and compression properties of 3D powder printed Ti-6Al-4V scaffolds with designed porosity: experimental and computational analysis, Mater. Sci. Eng. C Mater. Biol. Appl. 70 (Pt 1) (2017) 812–823.
[18] A. Souness, F. Zamboni, G.M. Walker, M.N. Collins, Influence of scaffold design on 3D printed cell constructs, J. Biomed. Mater. Res. B Appl. Biomater. 106 (2) (2018) 533–545.
[19] J.F.M. Ribeiro, S.M. Oliveira, J.L. Alves, A.J. Pedro, R.L. Reis, E.M. Fernandes, J.F. Mano, Structural monitoring and modeling of the mechanical deformation of three-dimensional printed poly(epsilon-caprolactone) scaffolds, Biofabrication 9 (2) (2017) 025015.
[20] S. Eshraghi, S. Das, Micromechanical finite-element modeling and experimental characterization of the compressive mechanical properties of polycaprolactone–hydroxyapatite composite scaffolds prepared by selective laser sintering for bone tissue engineering, Acta Biomater. 8 (8) (2012) 3138–3143.
[21] H. Zhao, W. Liang, A novel comby scaffold with improved mechanical strength for bone tissue engineering, Mater. Lett. 194 (2017) 220–223.
[22] A. Farzadi, V. Waran, M. Solati-Hashjin, Z.A.A. Rahman, M. Asadi, N.A.A. Osman, Effect of layer printing delay on mechanical properties and dimensional accuracy of 3D printed porous prototypes in bone tissue engineering, Ceram. Int. 41 (7) (2015) 8320–8330.
[23] D.A. Şerban, L. Marşavina, V. Silberschmidt, Behaviour of semi-crystalline thermoplastic polymers: experimental studies and simulations, Comput. Mater. Sci. 52 (1) (2012) 139–146.
[24] W. Shi, G. Liu, Z. Chen, Effects of the bulk compressibility on rubber isolator's compressive behaviors, Adv. Mech. Eng. 9 (5) (2017) 1687814017699352.
[25] A.A. Abbasi, M. Ahmadian, A. Alizadeh, S. Tarighi, Application of hyperelastic models in mechanical properties prediction of mouse oocyte and embryo cells at large deformations, ASME 2016 International Mechanical Engineering Congress and Exposition, American Society of Mechanical Engineers Digital Collection (2018).
[26] M.A. Velasco, C.A. Narvaez-Tovar, D.A. Garzon-Alvarado, Design, materials, and mechanobiology of biodegradable scaffolds for bone tissue engineering, Biomed Res. Int. 2015 (2015) 729076.
[27] J. Kadkhodapour, H. Montazerian, A. Darabi, A.P. Anaraki, S.M. Ahmadi, A.A. Zadpoor, S. Schmauder, Failure mechanisms of additively manufactured porous biomaterials: effects of porosity and type of unit cell, J. Mech. Behav. Biomed. Mater. 50 (2015) 180–191.
[28] J. Kadkhodapour, H. Montazerian, S. Raeisi, Investigating internal architecture effect in plastic deformation and failure for TPMS-based scaffolds using simulation methods and experimental procedure, Mater. Sci. Eng. C Mater. Biol. Appl. 43 (2014) 587–597.
[29] A. Farzadi, M. Solati-Hashjin, M. Asadi-Eydivand, N.A. Abu Osman, Effect of layer thickness and printing orientation on mechanical properties and dimensional accuracy of 3D printed porous samples for bone tissue engineering, PLoS One 9 (9) (2014) e108252.
[30] M. McCune, A. Shafiee, G. Forgacs, I. Kosztin, Predictive modeling of post bioprinting structure formation, Soft Matter 10 (11) (2014) 1790–1800.